

To be published in Nat. Mat.

**Direct observation of ferroelectric field effect and vacancy-controlled screening at the
BiFeO₃-La_xSr_{1-x}MnO₃ interface**

Young-Min Kim,^{1,2} Anna Morozovska,³ Eugene Eliseev,⁴ Mark P. Oxley,^{5,1} Rohan Mishra,^{5,1}
Sverre M. Selbach,⁶ Tor Grande,⁶ S. T. Pantelides,^{5,1}
Sergei V. Kalinin,⁷ and Albina Y. Borisevich¹

¹ Materials Sciences and Technology Division, Oak Ridge National Laboratory,
Oak Ridge, TN 37831, USA

² Division of Electron Microscopic Research, Korea Basic Science Institute,
Daejeon 305-333, Korea

³ Institute of Physics, National Academy of Sciences of Ukraine,
46, pr. Nauki, 03028 Kiev, Ukraine

⁴ Institute for Problems of Materials Science, National Academy of Sciences of Ukraine,
3, Krjijanovskogo, 03142 Kiev, Ukraine

⁵ Department of Physics and Astronomy, Vanderbilt University, Nashville, TN, USA

⁶ Department of Materials Science and Engineering, Norwegian University of Science and Technology, NO-7491 Trondheim, Norway

⁷ The Center for Nanophase Materials Sciences. Oak Ridge National Laboratory, Oak Ridge, TN 37831, USA

Development of interface-based magnetoelectric devices necessitates understanding of the polarization-mediated electronic phenomena and atomistic polarization screening mechanisms. In this work, LSMO-BFO interface is studied on a single unit-cell level via combination of direct order parameter mapping by scanning transmission electron microscopy with electron energy loss spectroscopy, demonstrating unexpected ~5% lattice expansion for regions with negative polarization charge with concurrent anomalous decrease of the Mn valence and change in oxygen K-edge intensity. We interpret this behavior as direct evidence for the screening by oxygen vacancies. The vacancies are predominantly accumulated at the second atomic layer of BFO, reflecting the difference of ionic conductivity between the components. This vacancy exclusion from the interface leads to formation of a tail-to-tail domain wall. At the same time, purely electronic screening is realized for positive polarization charge, with insignificant change in lattice and electronic properties. These studies demonstrate the highly non-trivial role of electrochemical phenomena on the functional properties of oxide interfaces, and underscore the need for studies using multiple characterization tools to reveal realistic picture. Furthermore, these behaviors suggest that vacancy dynamic and

exclusion can be a major player in determining interface functionality in oxide multilayers, opening pathway for completely new electronic device concepts.

Ferroelectric polarization control of the magnetic properties and metal-insulator transitions in strongly correlated oxides has remained a goal of active research for the past two decades.¹⁻⁴ This interest stems from applications including new classes of magnetoelectric and spintronic devices. At the same time, these systems offer a powerful platform to explore charge-controlled physics of transition metal oxides.⁵ These considerations have stimulated extensive effort in development of novel materials and heterostructures.^{2,6-8}

Development of interface-based magnetoelectric devices necessitates understanding of the atomistic mechanisms responsible for coupling between polarization, electronic, and spin structures.⁹⁻¹¹ Given the profound role of charge screening phenomena on the non-local thermodynamics of the ferroelectrics, such studies are also required to address long-standing issues such as stability of ferroelectric state in nanoscale systems and ferroelectric size effect. In addition to purely physical mechanisms, a number of recent studies suggest that redistribution of oxygen vacancies can play a significant role at oxide interfaces, necessitating these electrochemical degrees of freedom to be taken into account.¹²⁻¹⁶ Despite much effort, the direct observations of screening phenomena at ferroelectric-metal interface remained elusive, and the localization and state of vacancies remain unresolved. Notably, vacancy energies and interplay between vacancy and electronic behaviors¹⁷ are strongly affected by the nature of material. Hence nontrivial behaviors can be expected depending on vacancy vs. polarization localization, with simplest example of such effect being the dipole moment density, band offsets, and work functions at the interfaces.

Recent emergence of aberration corrected (scanning) transmission electron microscopy¹⁸ has enabled atomic-level observation of polarization dynamics at ferroelectric domain walls,¹⁹ interfaces,^{20,21} structural²² and topological defects.^{23,24} Here, we report observations of electronic and electrochemical effects induced by ferroelectric polarization using combined polarization mapping and electron energy loss spectroscopy. The direct observation of valence state change of marker atom provides evidence for ferroelectric field effect in oxide heterostructures. This behavior is further correlated with lattice strains, providing a comprehensive picture of polarization-dependent properties of ferroic interfaces and clearly differentiating non-trivial effects induced by vacancy exclusion.

As model system, we have chosen the BiFeO₃-(La_{0.67}Sr_{0.33})MnO₃ interface (BFO-LSMO). Previously, it was shown that the near-interface structure of BFO can change dramatically depending on sample thickness and polarization direction.²¹ Piezoresponse force microscopy²⁵⁻²⁷ imaging (PFM) of the as-prepared film illustrated presence of multiple antiparallel domains, and therefore multiple domain boundaries. Atomic-resolution studies of such boundaries in cross-section geometry can distinguish contributions to interface structure related to polarization orientation and polarization charge from those related to strain, octahedral tilts, and other polarization independent factors.

In this study, we investigated heterostructures of 50 nm BFO/5 nm LSMO/SrTiO₃ (STO) grown by pulsed laser deposition; STO substrate surface was TiO₂ terminated, which was previously shown to result in LSMO surface being MnO₂-terminated.^{28,29} Annular dark field (ADF) image of BFO-LSMO thin film interface along the [110] pseudo-cubic orientation in the vicinity of a ferroelectric domain boundary is given in Figure 1a. Interface

between the BFO and LSMO is clearly identifiable in the image, suggesting epitaxial interface of high quality.

We further used quantitative STEM^{21,23,30} for lattice spacing and polarization mapping. In this approach, 2-dimensional atom positions are determined numerically from the ADF images and then used to obtain structural parameters for every unit cell. The resulting measurements can have up to 2-4 picometer precision, providing high-veracity estimate of local bond length and hence oxidation states through Vegard effect³¹ (see Fig. S1 in Supplementary Information for quantification details). The map of the out-of-plane (c-axis) lattice spacings obtained from the image in Figure 1a is shown in Figure 1b. Note that about a half of the interface region shows a localized increase in the out-of plane lattice spacing in the first several atomic layers of BFO, similar to the earlier report.³² However, the other half of the image does not show any measurable lattice spacing anomaly, and the boundary between the two regions is quite abrupt. In the anomalous region, expansion was on average 5% of the equilibrium spacing, or 20 pm, which is a high value for an epitaxial perovskite and suggests either a significant built-in field (coupled to piezoelectric effect) or significant chemical inhomogeneity. Henceforth we will refer to the anomalous out-of-plane lattice spacing region as BFO (A)-LSMO, and the other region as BFO (B)-LSMO. The in-plane Bi-Bi spacing was also determined from Fig.1a, but it stayed virtually constant across the interface, which is expected due to epitaxial constraints.

Figure 1c shows the map of the out-of-plane off-center displacements of the Fe cations relative to Bi sublattice, which was shown to be proportional, and anticollinear, to BFO polarization.^{21,23} In the BFO (A) region with local lattice spacing expansion at the interface, Fe cations are displaced towards the interface, meaning that the polarization is oriented away

from it. In the BFO (B) region the polarization is pointing towards the interface. The one-to-one correspondence of the region with localized lattice expansion and region with polarization oriented towards the interface (Figures 1b and c) is striking, suggesting that the phenomena responsible for expansion are polarization mediated. Line profiles averaged over several atomic rows of out-of-plane and in-plane displacement maps for the two respective regions, BFO (A) and BFO (B), are overlaid on the Figure 1c. Note that in-plane displacements in both BFO regions are near zero, suggesting that [211] direction of the rhombohedral BFO is collinear with the incident electron beam.

On close examination of the out-of-plane displacement profile in the BFO (A) region, it can be seen that 2-3 layers directly at the interface become polarized in the opposite direction to that of the BFO film away from the interface; this observation is consistent with a previous report.³² The transition from unpolarized material on the LSMO side to saturated polarization on the BFO side happens over 3-4 unit cells, the same region where out-of-plane lattice parameter is increased (Fig.1c). For the out-of-plane displacement of the BFO (B), the polarization shows a gradual transition over the first 3-4 unit cells of BFO at the interface, and exhibits small positive value after the transition, which could be caused by a small rotation of the LSMO lattice out of alignment with the electron beam caused by the strain of the domain wall (e.g. similar to Ref. 33). These critical interface regions of the BFO film are indicated by pink shadow bands in both polarization graphs.

To fully analyze the phenomena at the interfaces, it is important to know the details of charge distribution, and therefore chemical profiles and oxidation states, of the constituent elements. To investigate these, we used Electron Energy Loss spectroscopy (EELS). The integrated intensity profiles for La M, Fe L, Mn L, Ti L, and O K edges across BFO–LSMO

and LSMO–STO interfaces confirming MnO₂ and TiO₂ terminations, respectively, are given in the Supplementary Figure S2. Comparison of the experimental profiles with the theoretical edge profiles calculated for the experimental thickness of 65 nm (Supplementary Figure S3) suggests a small degree of cation intermixing on the B site (~20%). Figures 2a,b show simultaneous ADF signal and color composites of Mn L and Fe L edge intensity maps obtained from 2D spectrum images across BFO (A) – LSMO and BFO (B) – LSMO interfaces, respectively. Some Mn/Fe intermixing is apparent in the first Fe layer inside BFO; however, at this level of Mn content it is still unlikely to dominate the behavior.

To assess electronic properties and chemical state of oxygen at the two interfaces, we then examined fine structure of the Fe L and Mn L edges. While Fe L edge can be fairly insensitive to chemical and electronic changes in the range relevant for perovskite thin films, Mn L edge fine structure was shown to reveal information about magnetic properties, charge carriers, and the oxygen (non)stoichiometry at the interface.³⁴⁻³⁹ Therefore, intermixing in this system provides us with an opportunity to monitor the environment in both BFO and LSMO by tracking Mn valence.

Bottom panels of the Figure 2a,b show average profiles of the integrated edge intensities along with profiles of L₃/L₂ ratios, which are indicative of the valence state of the corresponding cations.^{34,39} Reference L_{3,2} ratio values for different valence states of Fe and Mn are indicated as shadow bands.^{35,39} Experimental profiles show that away from the interface Fe and Mn have valence states of ~ +3, as expected for bulk BFO; for LSMO, a slightly higher value is expected for the full oxygen stoichiometry, suggesting that in our case LSMO is slightly oxygen poor and thus electron doped. With Fe, this behavior persists also in the interface region. However, Mn L_{3,2} ratio on the BFO side of the interface in BFO (A)

(Figure 2a) increases, indicating lower valence of Mn, while the valence of Mn diffusing into BFO (B) remains almost constant.

To complement this measurement, we examine O K EELS edge intensity across the two interfaces (Figure 3a). While the two profiles virtually overlap over most of the measurement range, right at the interface BFO (A)-LSMO shows measurably smaller intensity, indicating – qualitatively - that both the decreased oxidation state and lattice expansion could be driven by local oxygen vacancy injection. It is however very hard to draw reliable *quantitative* conclusions with respect to vacancy concentration from such data due to coherent nature of the EELS signal, which can vary greatly for different types of atoms, scattering angles, and sample thicknesses, producing complex delocalization behavior.^{12,36-38}

The observed behaviors at the BFO (A) interface strongly suggest screening by positively charged oxygen vacancies.^{40,41} Indeed, for polarization vector pointing away from the interface (case A) observed are (a) significant lattice expansion with the strains of the order of 5%, and (b) concomitant reduction of valence state for marker Mn atoms in BFO. In addition, oxygen K edge intensities suggest oxygen depletion at the interface. Vacancies in perovskite crystal lattice can give rise to lattice expansion, which in the case of cobaltites can be represented as a linear dependence of the lattice spacing on vacancy content.^{31,42,43} Using density functional theory, we have studied the effect of vacancy content on structure of BiFeO₃ (see Supplementary Information for details). For this material, the situation is complicated by the presence of ferroelectric polarization and several competing phases, including highly tetragonal form characterized by increased c/a ratio.⁴⁴ According to our results, lattice spacings in any one phase of the BiFeO₃ do not show a pronounced dependence on oxygen vacancy content (see Supplementary Table S1), however, the presence of

vacancies greatly reduces the penalty for formation of the highly tetragonal phase (see Supplementary Figure S4). Therefore, the observed local lattice expansion is likely caused by vacancy-induced local stabilization of the high c/a phase, with the overall effect being equivalent to Vegard expansion.

Since intermixed Mn is present in equal amounts in both BFO (A) and BFO (B) (Fig. 2), while vacancies are only observed in BFO (A), Mn doping per se cannot be the source of observed vacancy segregation. However, the reduced valence state of Mn is a signature of the oxygen vacancies. Mn^{2+} is a significantly larger cation (0.83 Å) than Fe^{3+} (0.645 Å) and the resulting Vegard expansion also contributes to the observed lattice expansion. In contrast, Mn in bulk BFO causes lattice contraction as it is primarily found as Mn^{3+} (0.645 Å) and Mn^{4+} (0.53 Å).⁴⁵ Local accumulation of vacancies at the BFO (A) interface is hence consistent with both the lower valence state of Mn (almost to the level of Mn^{2+}) in the EELS data (Fig. 2a) and the lattice expansion evident in Fig. 1b. In comparison, on the BFO (B) interface the screening is by electrons amply available from the LSMO, and neither lattice expansion nor reduced Mn valence is observed.

The analysis of the experimental data in Figs. 1 and 3 further illustrates the non-trivial effects of vacancy exclusion. We note that maximum expansion (and hence vacancy accumulation) is observed on the 2nd-3rd BFO layer, rather than directly at the interface. This is also the location where the formation of an interfacial tail-to-tail wall is observed. We ascribe this behavior to the *exclusion* effect. BFO is a good ionic conductor and can readily support oxygen non-stoichiometry.^{46,47} Based on the experimental data we argue that oxygen vacancies segregate at the near-surface layer of BFO, but not exactly at the surface, effectively forming a Stern-like double layer. At the same time, the ferroelectric distortion can

penetrate into the LSMO region as shown by Tagantsev.⁴⁸ This mismatch in spatial localization between vacancies and polarization leads to the presence of the inverse depolarization field, and hence formation of a polarization wave as observed in Fig. 1c.

To analyze screening phenomena in LSMO/BFO system and to establish polarization behavior in domains A and B as well as at the domain wall-interface junction and the space charge density at the (half)metal /ferroelectric interface, we use Landau-Ginzburg-Devonshire (LGD) theory coupled with electrostatics equations (see Refs. ^{49,50}). The geometry of the problem is shown in **Figure 4a**, and corresponding constitutive equations are described in Supplementary Information. The approximate analytical expressions for the electric field, electrostatic potential, ferroelectric polarization component, mobile oxygen vacancies (donors) and electrons concentrations derived using perturbation approach using Fermi-Dirac statistics for electrons and Boltzmann approximation by Shenoy for vacancies.⁵¹ Note that this model, while mathematically complex, presents the simplest possible description for coupled polarization-mobile carrier problem, similar to earlier studies in the fields of ferroelectric-semiconductors⁵²⁻⁵⁵ and mixed electronic-ionic conductors.^{56,57} Once available, such model allows relevant materials parameters to be established within the postulated physical model as derived from experimental observations.

Out-of-plane lattice constant $c(x, z)$ is shown in **Figure. 4d** in the domains A, B far from the domain wall – surface junction. For domain A, where the vacancies are accumulated near the interface, $c(x, z)$ is maximal at the interface layer and decreases to the bulk value with z increase. Far from the interface, where the vacancies concentration is equal to the bulk value and the same in domains A and B, $c(x, z)$ are the same in A and B, namely, the saturating z -dependence is defined by the electrostriction terms proportional to $P_3^2(x, z)$. In-

plane lattice constant is constant for both domains due to the perfect epitaxy, i.e. $a(x, z) = a_{STO}$ and is equal to $3.905/\sqrt{2}$ nm. The calculated behavior of the lattice constants are in the semi-quantitative agreement with experimental results shown in **Fig. 3b**.

The interface dipole layer consists of electrons in the half-metal electrode, which are separated from the ionized vacancies at the effective distance approximately equal to the effective screening length in BFO. The effective dipole moment $P_d(x, z) \approx e(R_d + R_s)N_d^+(x, z)$ consists of electrons in the half-metal electrode, which are separated from the ionized vacancies at the effective distance $R_d + R_s$, R_d is the effective screening length in BFO. The “built-in” interface dipole affects on the polarization near the interface of the domain A and causes the polarization profile asymmetry as shown in the **Figure 4c**. The polarization profile asymmetry further leads to the domain wall bending effect, as illustrated in **Figure 4d**. Namely, the domain wall plane between A and B them could bend in the junction vicinity in order to increase the region B. Far from the interface, only the proper (rather low) conductivity exists in BFO, and the domain wall plane between the regions A and B remains flat. The calculated behavior of polarization is in the semi-quantitative agreement with experimental results shown in **Fig. 1c**.

To summarize, the interplay between polarization and electronic phenomena at the BFO-LSMO interface was explored using combination of direct structural and order parameter mapping by STEM, and chemical and valence state mapping with EELS. For polarization pointing towards the interface (inducing positive polarization charge), no changes in lattice spacing or valence states of constituent materials are detected, suggesting predominantly electronic screening. At the same time, for polarization pointing away from the

interface (inducing negative polarization charge), significant lattice expansion and local reduction of Mn was observed, indicative of screening by oxygen vacancies.

We demonstrate charge-induced interface reconstruction in the ferroelectric (BFO)/metallic ferromagnetic (LSMO) thin film structure and elucidate the atomic-scale mechanism responsible for the polarization induced by the field effect, offering a new paradigm for interface-based magnetoelectric and spintronic devices. Furthermore, the change in Mn valence state indicates a change in magnetic moment between two polarization states, originating from a modification in the spin exchange coupling at the interface by the electrostatic field effect.⁵⁸

These studies suggest a significant role of electrochemical phenomena at functional oxide interfaces. We argue that accumulation of vacancies observed at the interface in the present work will strongly affect the polarization switching phenomena, since switching process should be accompanied by the redistribution of the vacancies, either into the LSMO phase or within BFO matrix. Such process will necessarily be slow as limited by vacancy transport times, and will control switching kinetics. Furthermore, in very thin film the antiparallel domain orientations as observed in Figure 1 will result in nominally “zero” polarization states, in agreement with multiple anomalies reported for ferroelectric responses in thin films (relaxor-like behavior, etc).

Finally, these studies underscore the need for comprehensive atomic-scale characterization using multiple modalities of STEM/EELS including local crystallography and energy loss spectroscopy. Of significant interest will be combination of these studies with scanning tunneling microscopy based band structure profiling,^{59,60} which could provide a truly integrated picture of oxide behavior at interfaces.

Acknowledgements:

The work is supported in part (AYB, YMK, SVK, RM, STP) by Materials Science and Engineering Division, Office of Basic Energy Sciences of the US DOE and through a user project supported by Oak Ridge National Laboratory's Center for Nanophase Materials Sciences, which is sponsored at Oak Ridge National Laboratory by the Scientific User Facilities Division, Office of Basic Energy Sciences, U.S. Department of Energy. MPO acknowledges support from DOE grant DE-FG02-09ER46554. The authors thank Pu Yu (Tsinghua University, Beijing, China), Ying-Hao Chu (National Chiao Tung University, Hsinchu, Taiwan), and Ramamoorthy Ramesh (University of California Berkeley) for providing BiFeO₃ films for the study. ANM and EAE acknowledge the support via bilateral SFFR-NSF project, namely US National Science Foundation under NSF-DMR-1210588 and State Fund of Fundamental Research of Ukraine, grant UU48/002. This research used resources of the National Energy Research Scientific Computing Center, which is supported by the Office of Science of the US Department of Energy under Contract No.DE-AC02-05CH11231.

Materials:

BiFeO₃ (BFO) on La_{0.7}Sr_{0.3}MnO₃ (LSMO)/SrTiO₃ (STO) thin film heterostructures were grown by pulsed laser deposition (PLD) with reflection high-energy electron diffraction (RHEED) monitoring for atomic layer growth process. The grown BFO films on both LSMO layers (5 nm) were 50-nm thick. Atomically smooth TiO₂-terminated STO (100) substrates were first prepared by a combined HF-etching/annealing treatment. The STO substrates had vicinal angles of ~0.1°. The PLD growth using stoichiometric LSMO and BFO targets was performed by resorting to a KrF-excimer laser with a fluence of ~1.5 J/cm² and a repetition rate of 1 or 2 Hz for the growth of LSMO and BFO, respectively. During growth, the substrate was held at 750 °C, in an oxygen environment at 200 mTorr for LSMO, while for BFO the conditions were adjusted to 670 °C and 100 mTorr. RHEED analysis demonstrated intensity oscillations indicating a layer-by-layer growth mode without any island formation. After the growth, the heterostructures were slowly cooled to room temperature in 1 atm of oxygen at a rate of 5 °C/min to optimize the oxidation level.

Methods:*STEM, EELS and Image Simulation*

Cross-sectional samples oriented along the $\langle 110 \rangle$ pseudocubic direction for STEM analysis were prepared by conventional mechanical thinning, precision polishing, and ion milling. ADF STEM images and EELS spectrum images for samples were taken using a 300-kV aberration-corrected scanning transmission electron microscope (VG Microscopes HB603U equipped with Nion[®] aberration corrector) with a convergence semi-angle of 23 mrad for the incident electron probe and a Nion UltraSTEM operating at 100 kV, equipped with a cold

field emission electron gun and a corrector of third and fifth order aberrations. EELS experiments were carried out with a Gatan Enfina® spectrometer attached to the Nion UltraSTEM. The convergence semi-angle for the electron probe was 31 mrad and the EELS collection semi-angle 48 mrad. ADF signals for the samples were collected from the detector angle range of ~86 to 200 mrad. EELS SI data across the BFO-LSMO interfaces was acquired from 420 to 950 eV with 0.4 eV/ch and 0.5 s/pixel dwell time on a 14 x 38 spatial pixel grids. The thicknesses in the observed sample regions were ranging from 50 up to 70 nm and the spectroscopic data showed consistent results. The sample thicknesses were estimated by the intensity ratio between the plasmon loss and the zero loss peaks in EELS. Noise in the obtained STEM images was reduced by using maximum entropy method (DECONVHAADF software package by HREM Research Inc.). STEM ADF image simulation (Fig. S1) was carried out using QSTEM software package bases on multislice method.

References

1. Ahn, C.H., *et al.* Local, nonvolatile electronic writing of epitaxial $\text{Pb}(\text{Zr}_{0.52}\text{Ti}_{0.48})\text{O}_3/\text{SrRuO}_3$ heterostructures. *Science* **276**, 1100-1103 (1997).
2. Lee, J.H., *et al.* A strong ferroelectric ferromagnet created by means of spin-lattice coupling. *Nature* **466**, 954-U972 (2010).
3. Miller, S.L. & McWhorter, P.J. Physics of the ferroelectric nonvolatile memory field-effect transistor. *Journal of Applied Physics* **72**, 5999-6010 (1992).
4. Molegraaf, H.J.A., *et al.* Magnetoelectric Effects in Complex Oxides with Competing Ground States. *Advanced Materials* **21**, 3470 (2009).
5. Imada, M., Fujimori, A. & Tokura, Y. Metal-insulator transitions. *Reviews of Modern Physics* **70**, 1039-1263 (1998).
6. Bibes, M., Villegas, J.E. & Barthelemy, A. Ultrathin oxide films and interfaces for electronics and spintronics. *Advances in Physics* **60**, 5-84 (2011).
7. Cheng, G.L., *et al.* Sketched oxide single-electron transistor. *Nature Nanotechnology* **6**, 343-347 (2011).
8. Fiebig, M. Revival of the magnetoelectric effect. *Journal of Physics D-Applied Physics* **38**, R123-R152 (2005).
9. Burton, J.D. & Tsymbal, E.Y. Prediction of electrically induced magnetic reconstruction at the manganite/ferroelectric interface. *Physical Review B* **80**, 174406 (2009).
10. Rondinelli, J.M., Stengel, M. & Spaldin, N.A. Carrier-mediated magnetoelectricity in complex oxide heterostructures. *Nature Nanotechnology* **3**, 46-50 (2008).
11. Yamauchi, K., Sanyal, B. & Picozzi, S. Interface effects at a half-metal/ferroelectric junction. *Applied Physics Letters* **91**, 062506 (2007).
12. Brivio, S., *et al.* Effects of Au nanoparticles on the magnetic and transport properties of $\text{La}_{0.67}\text{Sr}_{0.33}\text{MnO}_3$ ultrathin layers. *Physical Review B* **81**, 094410 (2010).
13. Estrade, S., *et al.* Effect of the capping on the local Mn oxidation state in buried (001) and (110) $\text{SrTiO}_3/\text{La}_{2/3}\text{Ca}_{1/3}\text{MnO}_3$ interfaces. *Journal of Applied Physics* **110**, 103903-103905 (2011).
14. Ferguson, J.D., *et al.* Epitaxial Oxygen Getter for a Brownmillerite Phase Transformation in Manganite Films. *Advanced Materials* **23**, 1226 (2011).
15. Kim, Y., Disa, A.S., Babakol, T.E. & Brock, J.D. Strain screening by mobile oxygen vacancies in SrTiO_3 . *Applied Physics Letters* **96**, 251901 (2010).
16. Schneider, C.W., *et al.* The origin of oxygen in oxide thin films: Role of the substrate. *Applied Physics Letters* **97**, 192107 (2010).
17. Lankhorst, M.H.R., Bouwmeester, H.J.M. & Verweij, H. Use of the rigid band formalism to interpret the relationship between O chemical potential and electron concentration in $\text{La}_{1-x}\text{Sr}_x\text{CoO}_{3-\delta}$. *Physical Review Letters* **77**, 2989-2992 (1996).
18. Pennycook, S.J. & Nellist, P.D. *Scanning Transmission Electron Microscopy: Imaging and Analysis*, (Springer New York, 2011).
19. Jia, C.L., *et al.* Atomic-scale study of electric dipoles near charged and uncharged domain walls in ferroelectric films. *Nature Materials* **7**, 57-61 (2008).
20. Chisholm, M.F., Luo, W.D., Oxley, M.P., Pantelides, S.T. & Lee, H.N. Atomic-Scale Compensation Phenomena at Polar Interfaces. *Physical Review Letters* **105**, 197602 (2010).
21. Chang, H.J., *et al.* Atomically Resolved Mapping of Polarization and Electric Fields Across Ferroelectric/Oxide Interfaces by Z-contrast Imaging. *Advanced Materials* **23**, 2474 (2011).

22. Jia, C.L., *et al.* Effect of a Single Dislocation in a Heterostructure Layer on the Local Polarization of a Ferroelectric Layer. *Physical Review Letters* **102**, 117601 (2009).
23. Nelson, C.T., *et al.* Spontaneous Vortex Nanodomain Arrays at Ferroelectric Heterointerfaces. *Nano Letters* **11**, 828-834 (2011).
24. Jia, C.L., Urban, K.W., Alexe, M., Hesse, D. & Vrejoiu, I. Direct Observation of Continuous Electric Dipole Rotation in Flux-Closure Domains in Ferroelectric Pb(Zr,Ti)O₃. *Science* **331**, 1420-1423 (2011).
25. Gruverman, A. & Kholkin, A. Nanoscale ferroelectrics: processing, characterization and future trends. *Reports on Progress in Physics* **69**, 2443-2474 (2006).
26. Balke, N., Bdikin, I., Kalinin, S.V. & Kholkin, A.L. Electromechanical Imaging and Spectroscopy of Ferroelectric and Piezoelectric Materials: State of the Art and Prospects for the Future. *Journal of the American Ceramic Society* **92**, 1629-1647 (2009).
27. Kalinin, S.V., Morozovska, A.N., Chen, L.Q. & Rodriguez, B.J. Local polarization dynamics in ferroelectric materials. *Reports on Progress in Physics* **73**, 056502 (2010).
28. Kim, Y.-M., *et al.* Interplay of octahedral tilts and polar order in BiFeO₃ films. *Advanced Materials* **25**, 2497 (2013).
29. Yu, P., *et al.* Interface control of bulk ferroelectric polarization. *Proceedings of the National Academy of Sciences* **109**, 9710-9715 (2012).
30. Jia, C.L., *et al.* Unit-cell scale mapping of ferroelectricity and tetragonality in epitaxial ultrathin ferroelectric films. *Nature Materials* **6**, 64-69 (2007).
31. Kim, Y.M., *et al.* Probing oxygen vacancy concentration and homogeneity in solid-oxide fuel-cell cathode materials on the subunit-cell level. *Nat. Mater.* **11**, 888-894 (2012).
32. Borisevich, A.Y., *et al.* Suppression of Octahedral Tilts and Associated Changes in Electronic Properties at Epitaxial Oxide Heterostructure Interfaces. *Physical Review Letters* **105**, 087204 (2010).
33. Pruneda, J.M., *et al.* Ferrodistortive instability at the (001) surface of half-metallic manganites. *Physical Review Letters* **99**, 226101 (2007).
34. Botton, G.A., Appel, C.C., Horsewell, A. & Stobbs, W.M. Quantification of the EELS near-edge structures to study Mn doping in oxides. *Journal of Microscopy* **180**, 211-216 (1995).
35. Cavé, L., Al, T., Loomer, D., Cogswell, S. & Weaver, L. A STEM/EELS method for mapping iron valence ratios in oxide minerals. *Micron* **37**, 301-309 (2006).
36. Maurice, J.L., Imhoff, D., Contoury, J.P. & Colliex, C. Interfaces in {100} epitaxial heterostructures of perovskite oxides. *Philosophical Magazine* **86**, 2127-2146 (2006).
37. Oxley, M.P. & Pennycook, S.J. Image simulation for electron energy loss spectroscopy. *Micron* **39**, 676-684 (2008).
38. Samet, L., *et al.* EELS study of interfaces in magnetoresistive LSMO/STO/LSMO tunnel junctions. *European Physical Journal B* **34**, 179-192 (2003).
39. Wang, Z.L., Yin, J.S. & Jiang, Y.D. EELS analysis of cation valence states and oxygen vacancies in magnetic oxides. *Micron* **31**, 571-580 (2000).
40. de Jong, M.P., *et al.* Evidence for Mn²⁺ ions at surfaces of La_{0.7}Sr_{0.3}MnO₃ thin films. *Physical Review B* **71**, 014434 (2005).
41. de Jong, M.P., *et al.* Valence electronic states related to Mn²⁺ at La_{0.7}Sr_{0.3}MnO₃ surfaces characterized by resonant photoemission. *Physical Review B* **73**, 052403 (2006).
42. Adler, S.B. Chemical expansivity of electrochemical ceramics. *Journal of the American Ceramic Society* **84**, 2117-2119 (2001).
43. Chen, X.Y., Yu, J.S. & Adler, S.B. Thermal and chemical expansion of Sr-doped lanthanum cobalt oxide (La_{1-x}Sr_xCoO_{3-δ}). *Chemistry of Materials* **17**, 4537-4546 (2005).

44. Zeches, R.J., *et al.* A Strain-Driven Morphotropic Phase Boundary in BiFeO₃. *Science* **326**, 977-980 (2009).
45. Selbach, S.M., Tybell, T., Einarsrud, M.-A. & Grande, T. Structure and Properties of Multiferroic Oxygen Hyperstoichiometric BiFe_{1-x}Mn_xO_{3+δ}. *Chemistry of Materials* **21**, 5176-5186 (2009).
46. Masó, N. & West, A.R. Electrical Properties of Ca-Doped BiFeO₃ Ceramics: From p-Type Semiconduction to Oxide-Ion Conduction. *Chemistry of Materials* **24**, 2127-2132 (2012).
47. Yang, C.H., *et al.* Electric modulation of conduction in multiferroic Ca-doped BiFeO₃ films. *Nature Materials* **8**, 485-493 (2009).
48. Gerra, G., Tagantsev, A.K. & Setter, N. Ferroelectricity in asymmetric metal-ferroelectric-metal heterostructures: A combined first-principles-phenomenological approach. *Physical Review Letters* **98**, 207601 (2007).
49. Morozovska, A.N., *et al.* Finite size and intrinsic field effect on the polar-active properties of ferroelectric-semiconductor heterostructures. *Physical Review B* **81**, 205308 (2010).
50. Eliseev, E.A., *et al.* Surface effect on domain wall width in ferroelectrics. *Journal of Applied Physics* **106**, 084102 (2009).
51. Sheldon, B.W. & Shenoy, V.B. Space Charge Induced Surface Stresses: Implications in Ceria and Other Ionic Solids. *Physical Review Letters* **106**, 216104 (2011).
52. Eliseev, E.A., Morozovska, A.N., Svechnikov, G.S., Maksymovych, P. & Kalinin, S.V. Domain wall conduction in multiaxial ferroelectrics. *Physical Review B* **85**, 045312 (2012).
53. Fridkin, V.M. *Ferroelectric Semiconductors*, (Springer, New York, 1980).
54. Gureev, M.Y., Tagantsev, A.K. & Setter, N. Head-to-head and tail-to-tail 180 degrees domain walls in an isolated ferroelectric. *Physical Review B* **83**, 184104 (2011).
55. Vul, B.M., Guro, G.M. & Ivanchik, II. Encountering domains in ferroelectrics. *Ferroelectrics* **6**, 29-31 (1973).
56. Riess, I. I-V relations in semiconductors with ionic motion. *Journal of Electroceramics* **17**, 247-253 (2006).
57. Maier, J. Thermodynamics of Nanosystems with a Special View to Charge Carriers. *Advanced Materials* **21**, 2571-2585 (2009).
58. Vaz, C.A.F., *et al.* Origin of the Magnetoelectric Coupling Effect in Pb(Zr_{0.2}Ti_{0.8})O₃/La_{0.8}Sr_{0.2}MnO₃ Multiferroic Heterostructures. *Physical Review Letters* **104**, 127202 (2010).
59. Chien, T.Y., Liu, J.A., Chakhalian, J., Guisinger, N.P. & Freeland, J.W. Visualizing nanoscale electronic band alignment at the La_{2/3}Ca_{1/3}MnO₃/Nb:SrTiO₃ interface. *Physical Review B* **82**, 041101 (2010).
60. Huang, B.C., *et al.* Direct observation of ferroelectric polarization-modulated band bending at oxide interfaces. *Applied Physics Letters* **100**, 122903 (2012).

Captions to Figures

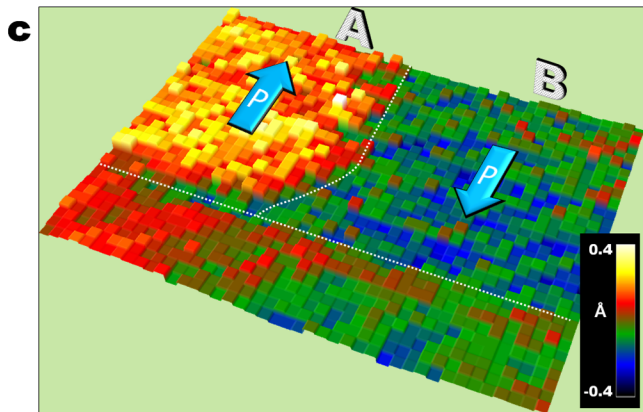
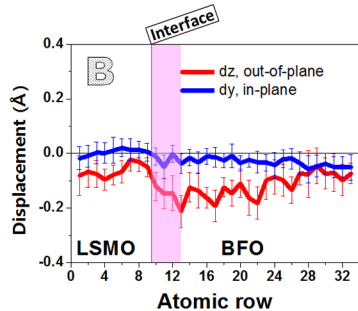
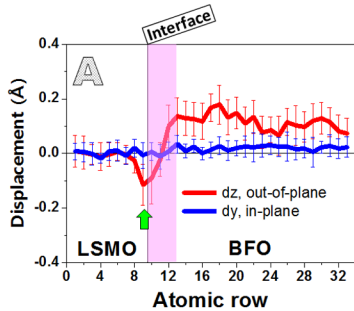
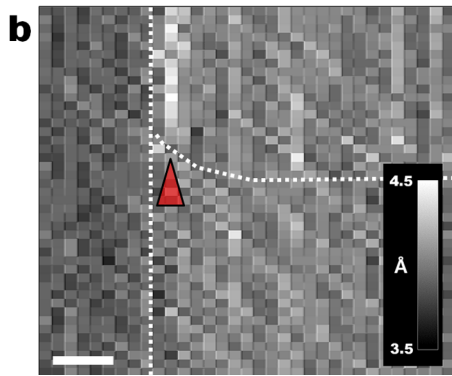
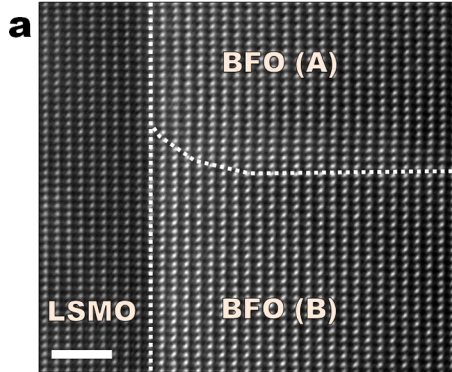
Figure 1 Lattice spacing and polarization changes at the interface of BFO-LSMO: (a) ADF image of [110] pseudo-cubic oriented BFO thin films grown on MnO₂-terminated LSMO. (b) Out-of-plane lattice spacing map and (c) polarization map of BFO film on LSMO showing antiparallel domain configuration. Corresponding B-site cation (Fe in BFO) displacement profiles (dz and dy for out-of-plane and in-plane directions, respectively) for the respective BFO domains are displayed as the topmost graphs (A and B) on the map, c. Note that those maps for lattice spacing and polarization changes were derived from quantitative atom position mapping for the ADF image shown in **a**.³² Scale bars are 2 nm.

Figure 2 Tracing averaged valence states of B-site cations at the two interfaces: The two top images on both sides are ADF signals and EELS maps of Fe (red) and Mn (green) L edges for the two interfaces (a) BFO (A)-LSMO and (b) BFO (B)-LSMO, respectively. Profiles of EELS L₃/L₂ intensity ratios of Fe (red line) and Mn (blue line) are given at the bottom of the respective panels; maxima on profiles correspond to atomic rows. The reference values of valence states corresponding to the EELS L_{2,3} edge ratios of Fe (yellow) and Mn (cyan) are marked as bands (the widths of the bands indicate experimental error) in the graphs.^{35,39} The detected EELS signal intensities of Fe and Mn are shown in the bottom part of the graphs as lines filled with orange stripes and light blue, respectively.

Figure 3. (a) Integrated intensity of O K edge across the two BFO-LSMO interfaces; note that for the BFO (A)-LSMO (red) the intensity at the interface is slightly lower than for the BFO (B)-LSMO interface (green). (b) Averaged profiles over the atomic rows of lattice spacing change maps for ADF STEM image in Figure 1a. Out-of-plane (a_x) and in-plane (a_y) lattice

spacings across the interfaces for the BFO (A)-LSMO and the BFO (B)-LSMO are displayed as red and green lines, respectively. The anomaly region with a bulge of the a_x lattice spacing of BFO at the interface is observed only in the BFO (A)-LSMO heterostructure combination (marked as arrow and pink shadow band).

Figure 4. (a) Geometry of the problem. Interface dipole P_d exists in the region $x > 0$, where ionized oxygen vacancies are accumulated. (b) Out-of-plane lattice constant $c(z)$ vs. the depth z far from the domain wall plane $x = 0$. (c) Polarization distribution vs. the distance z from the interface at different coordinates $x = \pm 1, \pm 3, \pm 30$ nm (numbers near the curves). (d) Domain wall bending effect caused by the interface dipole $P_d(x)$. Anisotropy $\gamma=1$, wall plane is $x = 0$, screening radius in the LSMO $R_s = 0.2$ nm, BFO screening length $R_d = 2$ nm, $L = 50$ nm, $E_d - E_F = -0.1$ eV, $L_c = 2$ nm. Other parameters corresponding to BFO/LSMO heterostructure are listed in the section C3 of the Supplementary Information.



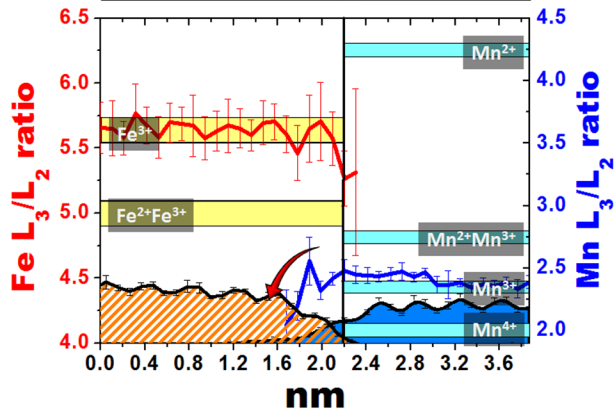
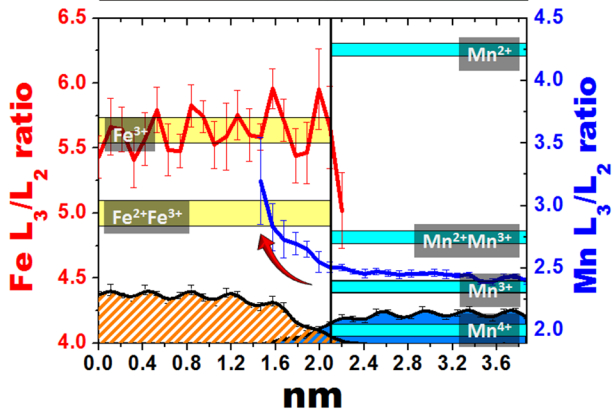
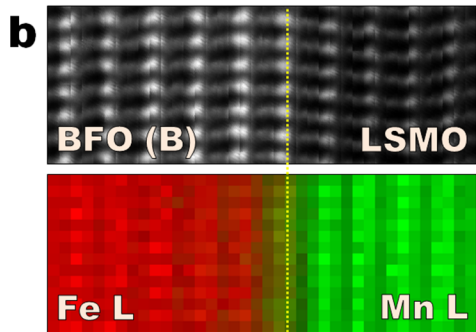
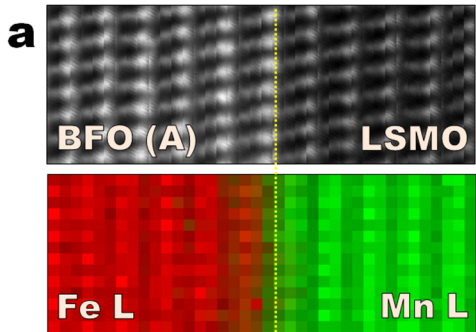


Figure 3. Kim *et al.*

